



Vortex-induced vibration control of a flexible circular cylinder using a nonlinear energy sink

Mingjie Zhang^{a,*}, Teng Wu^b, Ole Øiseth^a

^a Department of Structural Engineering, Norwegian University of Science and Technology, 7034, Trondheim, Norway

^b Department of Civil, Structural and Environmental Engineering, University at Buffalo, 14260, Buffalo, USA



ARTICLE INFO

Author keywords:

Vortex-induced vibration (VIV)
Circular cylinder
Vibration control
Nonlinear energy sink (NES)

ABSTRACT

A flexible structure immersed in a flowing fluid may exhibit vortex-induced vibration (VIV) dominated by either a fundamental or a higher-order mode depending on the flow velocity. Multimode coupled VIV may also exist if the structure presents closely spaced modes or significant nonlinear characteristics. While the traditional linear tuned mass damper designed for a single mode is ineffective for VIV control involving multiple modes, the nonlinear energy sink (NES) may work as a promising alternative due to its broadband vibration energy absorption capability. In this study, the governing equation of the coupled fluid-structure-NES system is first established based on a wake-oscillator model of the vortex-induced force. Then, a six-span continuous beam with an NES attachment is used as a case study to investigate the NES-based VIV control of a flexible structure with multiple degrees of freedom. The optimal NES is determined through a systematic parametric analysis considering both control effectiveness and robustness. Numerical results suggest that an NES designed for VIV control of the fundamental mode can also effectively control the VIVs of higher-order modes and that the controlling performance is robust to uncertainties of the stiffness and damping properties of both the primary structure and NES.

1. Introduction

As a typical flow-induced vibration, vortex-induced vibration (VIV) may occur for a circular cylinder as the periodic vortex-shedding frequency approaches one of its natural frequencies. Examples of cylindrical structures prone to VIVs include bridge cables (Chen et al., 2015), chimneys (Lupi et al., 2017), marine risers (Trim et al., 2005), and heat exchanger tubes (Païdoussis, 2006). A large number of fundamental studies have been devoted to testing the VIVs of different structures under various flow conditions, determining the dimensionless parameters dominating the VIV response, and understanding and modelling the complicated fluid-structure interaction phenomenon. Reviews on relevant topics can be found in several previous studies (Sarpkaya, 2004; Gabbai and Benaroya, 2005; Williamson and Govardhan, 2008; Païdoussis et al., 2010; Wu and Kareem, 2012).

Since VIV could influence the serviceability, reduce the fatigue life, and endanger the safety of a structure, it is important to take countermeasures to control the undesired VIV responses. Indeed, both active and passive VIV control measures have been intensely investigated in recent decades (e.g., Le Diouron et al., 2003; Zhu and Gao, 2017;

Hasheminejad et al., 2018; Xue et al., 2021). The applicability of active control measures is still quite limited due to the requirement for excessive power supply and complex actuation devices. Many passive control measures achieve VIV suppression of different structures by adding appendages to the surface of cylindrical structures, e.g., small rods, helical wires, fairing, and splitter plates (Zdravkovich, 1981; Demartino and Ricciardelli, 2017; Ishihara and Li, 2020; Zhang et al., 2021, 2022a). However, for some cases (e.g., the operational bridge hangers reported in Cantero et al. (2018)), installing these appendages requires high additional costs and long construction times. In addition, aerodynamic measures are not always the first choice considering the additional costs, construction times, and aesthetics. On the other hand, passive vibration absorbers have also been largely investigated as alternatives for VIV control. A tuned mass damper (TMD), which consists of a mass block attached to the primary structure through a linear spring and a linear damping element, is the most widely used passive vibration absorber. For example, TMD is often used to suppress the wind-induced vibrations of long-span bridges, tall buildings, and towers (Fujino and Yoshida, 2002; Dai et al., 2019). However, a TMD is often effective only for the specific single mode to which it is tuned, and the control

* Corresponding author.

E-mail addresses: mingjie.zhang@ntnu.no (M. Zhang), tengwu@buffalo.edu (T. Wu), ole.oiseth@ntnu.no (O. Øiseth).

efficiency is very sensitive to the detuning between the TMD frequency and natural frequency of the target structural mode. For a multiple-degree-of-freedom structure, the VIV may be dominated by either the fundamental mode or a higher-order mode depending on the flow velocity. Multimode coupled VIV may also exist if the structure presents closely spaced modes or significant nonlinear structural characteristics. Multiple TMDs are necessary in such cases, which not only increases the cost but also requires complicated optimization rules to design the TMD parameters (Xu et al., 2022).

In the past two decades, another type of passive vibration absorber, i.e., a nonlinear energy sink (NES), has been largely advanced due to its broadband vibration control capability. An NES usually consists of a mass block, a linear damping element, and an essentially nonlinear (e.g., a purely cubic) spring. The investigation of NESs was pioneered by Gendelman et al. (2001) and Vakakis et al. (2003), who provided the earliest numerical evidence that a cubic nonlinear oscillator attachment can passively absorb broadband vibration energy from the linear primary oscillator. Lee et al. (2005) and Kerschen et al. (2005, 2007) numerically and experimentally studied the vibration control of a multiple-degree-of-freedom system using a lightweight and ungrounded NES. They showed that the NES is capable of exhibiting isolated resonance captures with different structural modes. In the case of multimode coupled vibrations, an NES can absorb energy from various modes successively through resonance capture cascades (i.e., transient resonances of the NES with several modes of the primary structure). Vibration control using NESs has attracted the interest of researchers from multiple disciplines, e.g., aerospace engineering (Lee et al., 2008) and civil engineering (Wierschem et al., 2014; Wang et al., 2015, 2020). Tumkur et al. (2013a) proposed suppressing the VIV of an elastically mounted rigid circular cylinder with an NES and numerically simulated the suppression effects at low Reynolds numbers. They showed that an NES with a mass ratio (between the NES and cylinder) of 11.0% could achieve a 78% reduction in the vibration amplitude. Tumkur et al. (2013b) further examined two energy transfer mechanisms responsible for passive VIV control based on computational fluid dynamic simulations and a reduced-order model for the coupled fluid-cylinder-NES system. Based on a series of computational fluid dynamic simulations, Mehmood et al. (2014) found that the response of the cylinder-NES system may depend on the initial condition and that the control effectiveness increases significantly while the NES mass ratio was increased from 2.0% to 3.0%. Accordingly, they suggested that the NES mass ratio should be larger than a critical value to achieve effective VIV control. More recently, the influences of the NES parameters, i.e., mass, stiffness, and damping, on VIV suppression of an elastically mounted rigid circular cylinder were investigated numerically by Dai et al. (2017) and Chen et al. (2020, 2021).

Despite several studies on VIV control of a circular cylinder using an NES, these existing studies considered a cylinder-NES system with an elastically mounted rigid circular cylinder. To the best of the authors' knowledge, the potential of an NES for higher-order mode and multimode VIV control of a multiple-degree-of-freedom flexible cylinder has never been investigated. In addition, the control effectiveness of the NES was not fully exploited because the NES stiffness and damping properties in these existing studies were chosen without systematic optimization. The NES considered in existing studies was usually with a large mass ratio (>2.0%), which may be uneconomic or impractical for VIV control of large-scale structures. The main novelty of this study lies in some numerical evidence showing the suppression effect on VIVs of a flexible circular cylinder using an NES. The governing equation of the coupled fluid-cylinder-NES system is established based on a reduced modal representation of the cylinder displacement and a wake-oscillator model of the vortex-induced force (Facchinetto et al., 2004). The NES is considered as a lumped mass suspended inside the circular cylinder through a cubic stiffness and a linear damping element in parallel. The effectiveness of an NES for VIV control of a flexible structure is demonstrated by a case study of a six-span continuous beam. The

equations of motion of the coupled fluid-cylinder-NES system are numerically integrated using a nonlinear Newmark method (Krenk, 2009). Due to the absence of design formulas for NES optimization in VIV control, the optimal NES stiffness and damping properties for a specific mass ratio are determined through a parametric analysis. The effectiveness of a TMD with the same mass ratio (between damper and cylinder) is also analysed to highlight the superiority of the NES. The robustness of the NES to uncertainties in the damping and stiffness properties of the cylinder and the NES is investigated. Finally, the effect of NES mass on the control performance and the applicability of the single-mode approximation of the cylinder response (which is often adopted in VIV analysis of a structure with a large mass ratio between the structure and displaced fluid) for the cylinder-NES system is examined.

2. Mathematical modelling of the fluid-cylinder-damper system

A flexible circular cylinder immersed in a smooth uniform flow with a single damper (i.e., an NES or a TMD) attachment is considered. The layout of the cylinder-damper system is provided schematically in Fig. 1, in which x and y represent the streamwise and transverse coordinates, respectively, and D represents the diameter of the cylinder. The cylinder can vibrate in the transverse direction, while the streamwise vibration is not considered. The flow-induced force on the damper is not considered since the damper is placed inside the cylinder. A cover (shown in pink in Fig. 1) can be used to protect the damper if any internal flow exists inside the circular cylinder. The ratio between the damper mass and cylinder mass is assumed to be very small (<1.5%), and hence, the attachment of the damper does not cause any significant changes to the static equilibrium and modal properties of the flexible cylinder.

Considering a uniform cylinder with a mass m_c per unit span length, an elastic modulus E , the second moment of area I , and a viscous damping coefficient c_c , the partial differential equations of motion of the cylinder-damper system can be expressed as

$$EI \frac{\partial^4 y_c(z, t)}{\partial z^4} + m_c \frac{\partial^2 y_c(z, t)}{\partial t^2} + c_c \frac{\partial y_c(z, t)}{\partial t} + F_d(t) \delta(z - z_d) = F_{\text{flow}}(z, t) \quad (1a)$$

$$m_d \ddot{y}_d(t) - F_d(t) = 0 \quad (1b)$$

where $z = 0 \sim L$ represents the coordinate along the cylinder length, L represents the total length of the cylinder, $y_c(z, t)$ is the transverse displacement of the cylinder, $y_d(t)$ is the transverse displacement of the damper, $F_d(t)$ is the force exerted on the cylinder by the damper, $F_{\text{flow}}(z, t)$ is the vortex-induced force acting on the cylinder, δ is the Dirac delta function, z_d is the spanwise coordinate of the suspending point of the damper on the cylinder, and the overdot represents the derivative with respect to time t .

The vortex-induced force is simulated using the wake oscillator model as (Facchinetto et al., 2004)

$$F_{\text{flow}}(z, t) = \frac{1}{4} \rho U^2 D C_{L0} q(z, t) - \gamma \omega_f \rho D^2 \frac{\partial y_c(z, t)}{\partial t} \quad (2)$$

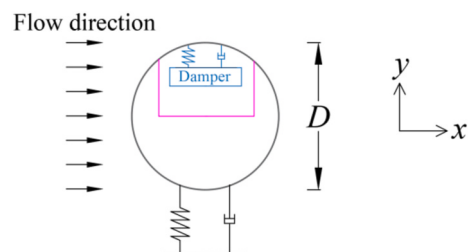


Fig. 1. Schematic diagram of a fluid-cylinder-damper system.

$$\frac{\partial^2 q(z, t)}{\partial t^2} + \epsilon \omega_f [q^2(z, t) - 1] \frac{\partial q(z, t)}{\partial t} + \omega_f^2 q(z, t) = \frac{A}{D} \frac{\partial^2 y_c(z, t)}{\partial t^2} \quad (3)$$

where ρ is the air density, U is the flow velocity, C_{L0} is the reference lift coefficient, $q(z, t)$ is the dimensionless wake variable, γ is the fluid-added damping coefficient, ϵ and A are dimensionless parameters determining the coupling effect between fluid and cylinder vibration, $\omega_f = 2\pi St(U/D)$ is the vortex-shedding frequency (in rad/s) according to the Strouhal law, and St is the Strouhal number. The same model was utilized by Dai et al. (2017) to calculate the VIV response of an elastically mounted rigid circular cylinder with an NES attachment. Indeed, since the wake-oscillator model cannot fully capture the nonlinear vortex-induced effect, the model cannot simulate the VIV responses with high accuracy while it can qualitatively reproduce the overall trend of the VIV responses, as demonstrated by Facchinetto et al. (2004) and Dai et al. (2017). Furthermore, Violette et al. (2007) showed that the wake-oscillator model can qualitatively simulate the multi-mode VIVs of a flexible circular cylinder. Hence, the present numerical simulation should be able to qualitatively investigate the VIV response of the cylinder-damper system and study the VIV control effect of the NES. On the other hand, the force decomposition models (with frequency-dependent force coefficients) can calculate the VIV responses of a cylinder-damper system with higher accuracy (Zhang et al. 2019, 2020, 2022b). However, these models assume the VIV is a mono-component vibration, making the models only applicable for elastically mounted rigid circular cylinders and hence they are not appropriate for the purpose of this paper.

The cylinder displacement and wake variable are decomposed into their modal components following Keber and Wiercigroch (2008) and Pavlovskaia et al. (2016).

$$y_c(z, t) = \sum_{n=1}^N \varphi_n(z) \eta_n(t) \quad (4a)$$

$$q(z, t) = \sum_{n=1}^N \varphi_n(z) q_n(t) \quad (4b)$$

where $\varphi_n(z)$ ($n = 1 \sim N$) is the mode shape of the flexible circular cylinder, N is the total number of modes considered in the simulation, and $\eta_n(t)$ and $q_n(t)$ are the n th-order modal coordinates of cylinder displacement and wake variable, respectively. The mode shapes satisfy the following orthogonality property

$$\int_0^L \varphi_n(z) \varphi_k(z) dz = 0, \quad n \neq k \quad (5)$$

By assuming that the damper is an NES with a cubic stiffness and a linear damping element, the force exerted on the cylinder by the NES can be expressed as

$$F_d(t) = c_d [\dot{y}_c(z_d, t) - \dot{y}_d(t)] + k_d [y_c(z_d, t) - y_d(t)]^3 \quad (6)$$

where c_d and k_d are the damping coefficient and stiffness coefficient of the NES, respectively.

Substituting Equations (2)–(4) and (6) into Equation (1), the partial differential equations of motion of the cylinder-NES system become

$$\begin{aligned} \sum_{n=1}^N \varphi_n(z) \ddot{q}_n(t) + \epsilon \omega_f \left[\left(\sum_{n=1}^N \varphi_n(z) q_n(t) \right)^2 - 1 \right] \sum_{n=1}^N \varphi_n(z) \dot{q}_n(t) + \omega_f^2 \sum_{n=1}^N \varphi_n(z) q_n(t) \\ \times \sum_{n=1}^N \varphi_n(z) q_n(t) = \frac{A}{D} \sum_{n=1}^N \varphi_n(z) \ddot{\eta}_n(t) \end{aligned} \quad (7b)$$

$$m_d \ddot{y}_d(t) - c_d \left[\sum_{n=1}^N \varphi_n(z_d) \dot{\eta}_n(t) - \dot{y}_d(t) \right] - k_d \left[\sum_{n=1}^N \varphi_n(z_d) \eta_n(t) - y_d(t) \right]^3 = 0 \quad (7c)$$

where the prime represents the derivative with respect to coordinate z .

Multiplying Equation (7) by the mode shape $\varphi_k(z)$ and integrating over the cylinder length, the ordinary differential equations of motion of the cylinder-NES system can be obtained as

$$\begin{aligned} m_k \left[\ddot{\eta}_k(t) + 4\pi \xi_k f_k \dot{\eta}_k(t) + (2\pi f_k)^2 \eta_k(t) \right] + \left\{ c_d \left[\sum_{n=1}^N \varphi_n(z_d) \dot{\eta}_n(t) - \dot{y}_d(t) \right] \right. \\ \left. + k_d \left[\sum_{n=1}^N \varphi_n(z_d) \eta_n(t) - y_d(t) \right]^3 \right\} \varphi_k(z_d) = \frac{1}{4} \rho U^2 D C_{L0} q_k(t) \int_0^L \varphi_k^2(z) dz \\ - \gamma \omega_f \rho D^2 \dot{\eta}_k(t) \int_0^L \varphi_k^2(z) dz \end{aligned} \quad (8a)$$

$$\ddot{\eta}_k(t) + \frac{\epsilon \omega_f \int_0^L [\sum_{n=1}^N \varphi_n(z) q_n(t)]^2 \sum_{n=1}^N \varphi_n(z) \dot{q}_n(t) \varphi_k(z) dz}{\int_0^L \varphi_k^2(z) dz} - \epsilon \omega_f \dot{\eta}_k(t) \\ + \omega_f^2 q_k(t) = \frac{A}{D} \ddot{\eta}_k(t) \quad (8b)$$

$$m_d \ddot{y}_d(t) - c_d \left[\sum_{n=1}^N \varphi_n(z_d) \dot{\eta}_n(t) - \dot{y}_d(t) \right] - k_d \left[\sum_{n=1}^N \varphi_n(z_d) \eta_n(t) - y_d(t) \right]^3 = 0 \quad (8c)$$

where $m_k = m_c \int_0^L \varphi_k^2(z) dz$, ξ_k , and f_k are the modal mass, damping ratio, and natural frequency (in Hz) of the k th-order mode of the circular cylinder, respectively.

If the damper is a TMD with a linear stiffness and a linear damping element, the force exerted on the cylinder by the TMD can be expressed as

$$F_d(t) = c_d [\dot{y}_c(z_d, t) - \dot{y}_d(t)] + k_d [y_c(z_d, t) - y_d(t)] \quad (9)$$

The ordinary differential equations of motion of the cylinder-TMD system can be obtained as

$$\begin{aligned} EI \sum_{n=1}^N \varphi_n'''(z) \eta_n(t) + m_c \sum_{n=1}^N \varphi_n(z) \ddot{\eta}_n(t) + c_c \sum_{n=1}^N \varphi_n(z) \dot{\eta}_n(t) + \left\{ c_d \left[\sum_{n=1}^N \varphi_n(z_d) \dot{\eta}_n(t) - \dot{y}_d(t) \right] \right. \\ \left. + k_d \left[\sum_{n=1}^N \varphi_n(z_d) \eta_n(t) - y_d(t) \right]^3 \right\} \delta(z - z_d) = \frac{1}{4} \rho U^2 D C_{L0} \sum_{n=1}^N \varphi_n(z) q_n(t) \\ - \gamma \omega_f \rho D^2 \sum_{n=1}^N \varphi_n(z) \dot{\eta}_n(t) \end{aligned} \quad (7a)$$

$$\begin{aligned} m_k \left[\ddot{\eta}_k(t) + 4\pi\xi_k f_k \dot{\eta}_k(t) + (2\pi f_k)^2 \eta_k(t) \right] + \left\{ c_d \left[\sum_{n=1}^N \varphi_n(z_d) \dot{\eta}_n(t) - \dot{y}_d(t) \right] \right. \\ \left. + k_d \left[\sum_{n=1}^N \varphi_n(z_d) \eta_n(t) - y_d(t) \right] \right\} \varphi_k(z_d) = \frac{1}{4} \rho U^2 D C_{L0} q_k(t) \int_0^L \varphi_k^2(z) dz \\ - \gamma \omega_f \rho D^2 \dot{\eta}_k(t) \int_0^L \varphi_k^2(z) dz \end{aligned} \quad (10a)$$

$$\begin{aligned} \dot{\eta}_k(t) + \frac{\varepsilon \omega_f \int_0^L [\sum_{n=1}^N \varphi_n(z) q_n(t)]^2 \sum_{n=1}^N \varphi_n(z) \dot{q}_n(t) \varphi_k(z) dz}{\int_0^L \varphi_k^2(z) dz} - \varepsilon \omega_f \dot{q}_k(t) \\ + \omega_f^2 q_k(t) = \frac{A}{D} \ddot{\eta}_k(t) \end{aligned} \quad (10b)$$

$$m_d \ddot{y}_d(t) - c_d \left[\sum_{n=1}^N \varphi_n(z_d) \dot{\eta}_n(t) - \dot{y}_d(t) \right] - k_d \left[\sum_{n=1}^N \varphi_n(z_d) \eta_n(t) - y_d(t) \right] = 0 \quad (10c)$$

3. VIV control of a flexible circular cylinder

3.1. Model of a flexible circular cylinder

As shown in Fig. 2, the considered flexible circular cylinder is a six-span continuous beam with a consistent span length of 1 m. All supports are assumed to be pinned. Unless otherwise stated, the following structural properties are adopted for the uniform circular cylinder: $D = 0.02$ m, $m_c = 0.044$ kg/m, and $EI = 1.7815$ N/m. The resulting modal masses and modal frequencies of the first six modes are listed in Table 1. The corresponding mode shapes are presented in Fig. 3, in which the circles represent the supporting points of the beam. The mass ratio between the circular cylinder and displaced fluid is $m_c / (\frac{\pi \rho D^2}{4}) = 114$. The beam can be considered as a prototype heat exchanger tube in gas flow or an aeroelastic model of a pipeline bridge girder. Since the six-span beam has several closely-spaced modes, it is appropriate for investigating the control performance of an NES for several modes. A zero structural damping coefficient (i.e., $c_c = 0$) is considered to highlight the control performance of the NES. Further simulations show that the general conclusions of this study are independent of the structural damping coefficient. Following Facchinetto et al. (2004), the constants of the wake oscillator model are adopted as $C_{L0} = 0.3$, $\gamma = 0.8$, $\varepsilon = 0.3$, $A = 12$, and $St = 0.2$. It is noted that the vortex-induced forces are constant along the cylinder axis in the present simulation, while the forces can be strongly influenced by the local irregularities of the surface for real cylinders (Matteoni and Georgakis, 2012; Benidir et al., 2015; Demartino and Ricciardelli, 2018).

3.2. VIV response of the uncontrolled cylinder

The VIV response of the uncontrolled circular cylinder is first presented. The equations of motion of the coupled fluid-cylinder system are numerically integrated using the nonlinear Newmark method (Krenk, 2009). The simulations are performed over a flow velocity range of $U = 0.7$ – 2.5 m/s, which covers the lock-in range of the first six modes. For

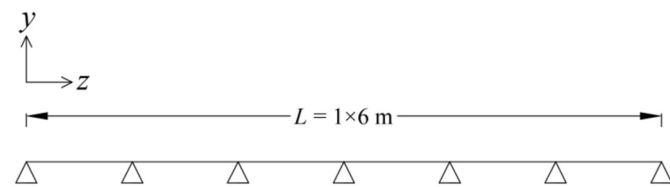


Fig. 2. Span arrangement of the flexible cylinder.

each flow velocity, the initial displacements of all considered modes are $\eta_k(0) = 0.01D$, while the initial velocities are 0. The simulation is performed for a sufficiently long time to obtain the steady-state response of the coupled system. To investigate the effect of multimode coupling on the VIV response, the equations of motion are integrated by considering different choices of N (i.e., mode number considered in the simulation). In the single-mode analysis (i.e., $N = 1$), a mode-by-mode analysis is conducted since VIV is dominated successively by different modes with increasing flow velocity.

Fig. 4 presents the root-mean-square (RMS) values of the steady-state displacements $RMS(y_c)/D$ at various reduced flow velocities $U/(f_1 D)$, in which the results of different choices of N are compared. The magenta lines on the right part of the figure represent the RMS displacements along the cylinder length. The RMS displacements at some segments are shown in negative to facilitate identifying the dominant mode (since the VIV response at each reduced velocity is dominated by a single mode, the displacements along the cylinder follow the mode shape of the dominant mode). The circles on the magenta lines represent the supporting points, and the squares indicate the locations with the largest RMS displacements. The RMS displacements on the left part of the figure are the values of the locations with the largest displacements. For example, the results represent the RMS displacements at $z = 0.5, 1.5, 2.5, 3.5, 4.5$, or 5.5 m if the VIV response is dominated by Mode 1.

Fig. 4 shows that large-amplitude VIVs occur in the reduced velocity range of $U/(f_1 D) = 4.5$ – 12.0 . Generally, the VIV response of the uncontrolled cylinder is successively dominated by each separate mode with increasing flow velocity. In the single-mode analysis, there is an overlap between the lock-in ranges of Mode 1 and Mode 2 due to their very close frequencies. In the multimode analysis, the transition from 1st-mode VIV to 2nd-mode VIV is characterized by a jump in the RMS displacement. The same is true for Mode 5 and Mode 6. The RMS displacements of the single-mode analysis are lower than the results of the multimode analysis in some specific ranges of reduced flow velocities. The difference is due to the multimode coupling effect induced by the aeroelastic nonlinearity, which is discussed later in this subsection. The results of the six-mode analysis agree very well with those of the ten-mode analysis. Hence, the results for $N = 6$ are adopted as references in the following parts.

Typical displacement time histories and Fourier spectra of the uncontrolled circular cylinder are presented in Fig. 5. The Fourier spectra are calculated based on the steady-state displacement signals. The VIV responses in Fig. 5(a, b, c, and d) are dominated by the vibrations of Mode 1, Mode 2, Mode 4, and Mode 5, respectively. It is noted that the 1st-mode vibration in Fig. 5(b) continues to decay with increasing time, and the vibration reduces to zero at approximately $t = 150$ s. The VIV response of the uncontrolled cylinder is dominated by a single mode because, in the lock-in range for a specific mode, the surrounding fluid provides a negative aeroelastic damping effect for this specific mode, while it provides positive aeroelastic-damping effects for other modes. As shown in Fig. 5(a) and (c), the steady-state VIV responses at $U/(f_1 D) = 5.0$ and 7.7 consist only of the vibrations of the dominant modes, while the displacements of other modes decay to zero with increasing time. The Fourier spectra in Fig. 5(a and c) show that the cylinder exhibits a quasi-harmonic vibration with a single dominant frequency. At these two reduced velocities, the steady-state RMS displacements from

Table 1
Modal masses and frequencies of the flexible cylinder.

Mode	Modal mass (kg)	Frequency (Hz)
1	0.1320	10.00
2	0.0704	10.77
3	0.0850	12.81
4	0.1159	15.61
5	0.0600	18.70
6	0.0591	21.44

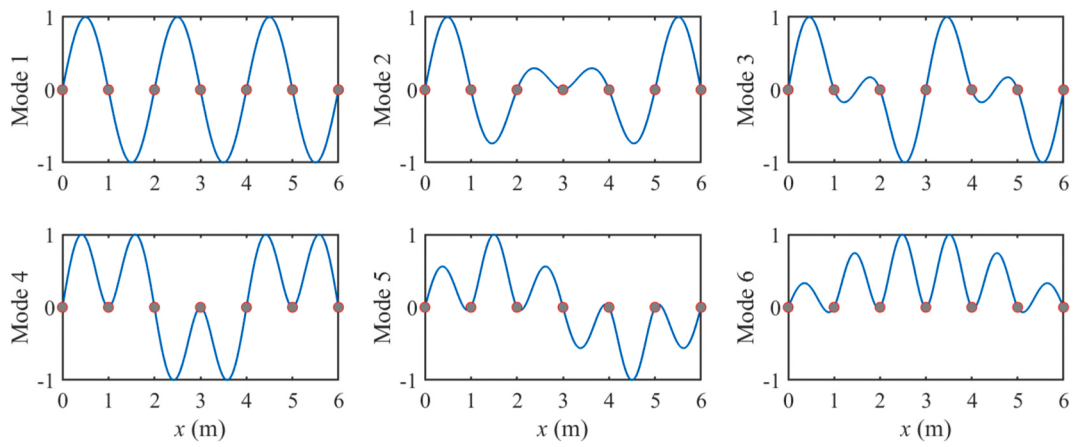


Fig. 3. Mode shapes of the flexible cylinder (note: the circles represent the supporting points).

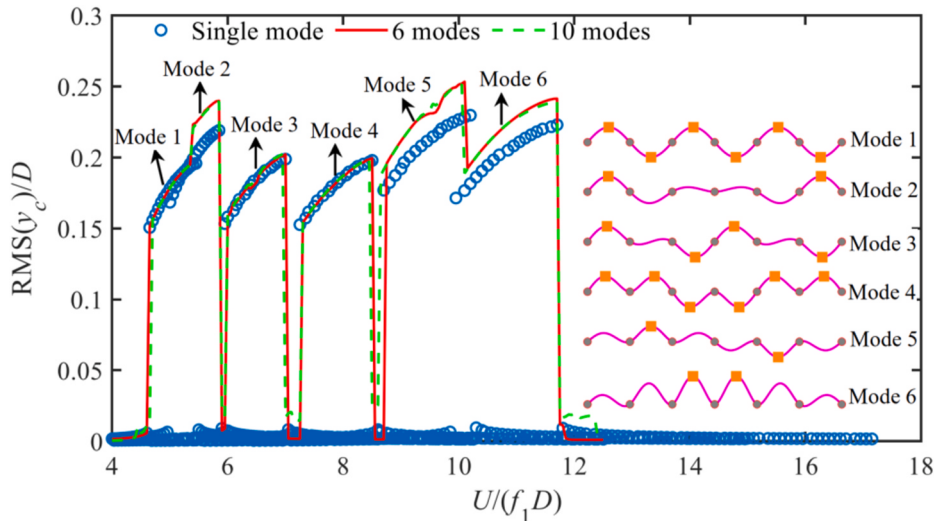


Fig. 4. Steady-state RMS displacements of the uncontrolled cylinder (note: the magenta lines represent the RMS displacements along the cylinder length, the circles indicate the supporting points, and the squares indicate the locations with the largest RMS displacements).

the single-mode analysis are almost consistent with the results from the multimode analysis, as confirmed in Fig. 4. It is noted that $U/(f_1 D) = 5.0$ lies within the overlap between the lock-in ranges of Mode 1 and Mode 2 according to the single-mode analysis (see Fig. 4). However, the multimode analysis predicts a Mode 1-dominated response, indicating that the vortex shedding is synchronized to the vibration of Mode 1, and hence Mode 2 of the circular cylinder is not excited.

On the other hand, as shown in Fig. 5(b), the steady-state VIV response at $U/(f_1 D) = 5.8$ includes not only the vibration of the dominant mode (i.e., Mode 2) but also a secondary component of another mode (i.e., Mode 4). The same is true for the steady-state VIV response at $U/(f_1 D) = 9.2$, as presented in Fig. 5(d). As a result, the steady-state RMS displacements at these two reduced velocities from the single-mode analysis are slightly lower than the results from the multimode analysis, as compared in Fig. 4. The Fourier spectra in Fig. 5(b and d) show that the frequency of the secondary component is consistent with the frequency of the dominant component. This is because the vortex shedding is synchronized to the vibration of the dominant mode, and hence, the vibration of the secondary component is a forced vibration following the vortex-shedding frequency. As shown by the coupled equations of motion of the uncontrolled cylinder [i.e., Eq. (8) without the terms related to the damper], the only term that couples the motions of various modes is the cubic nonlinear term in the wake oscillator, i.e., the 2nd term on the left-hand side of Eq. (8b). The significance of

coupling between two modes (e.g., Mode k and Mode n) is hence determined by the quantity of $\int_0^L \varphi_n^3(z) \varphi_k(z) dz / \int_0^L \varphi_k^2(z) dz$. As an example, the coupling quantities induced by Mode 2 are $\int_0^L \varphi_2^3(z) \varphi_k(z) dz / \int_0^L \varphi_k^2(z) dz = 0, 0.60, 0, 0.157, 0$ and 0 for $k = 1, 2, 3, 4, 5$, and 6, respectively. Hence, the VIV response in the lock-in range of Mode 2 is accompanied by a secondary component of Mode 4, as confirmed in Fig. 5(b).

3.3. Performance comparison of a TMD and an NES

An NES is then introduced to control the large-amplitude VIVs of the example flexible cylinder. As schematically shown in Fig. 1, the considered NES is a lumped mass suspended inside the circular cylinder through a cubic stiffness and a linear damping element in parallel. Unless otherwise stated, the NES is suspended on the beam at $z = 0.5$ m (where the displacement of Mode 1 achieves the largest value), and the mass ratio is $R_m = m_d / (m_c L) = 0.80\%$. A TMD with the same mass ratio is also studied to compare the performances of the NES and TMD.

The stiffness and damping properties of the dampers should be designed appropriately because their performances depend significantly on these properties. Analytical treatment of the cylinder-NES system is complicated due to the essentially nonlinear nature of the NES stiffness.

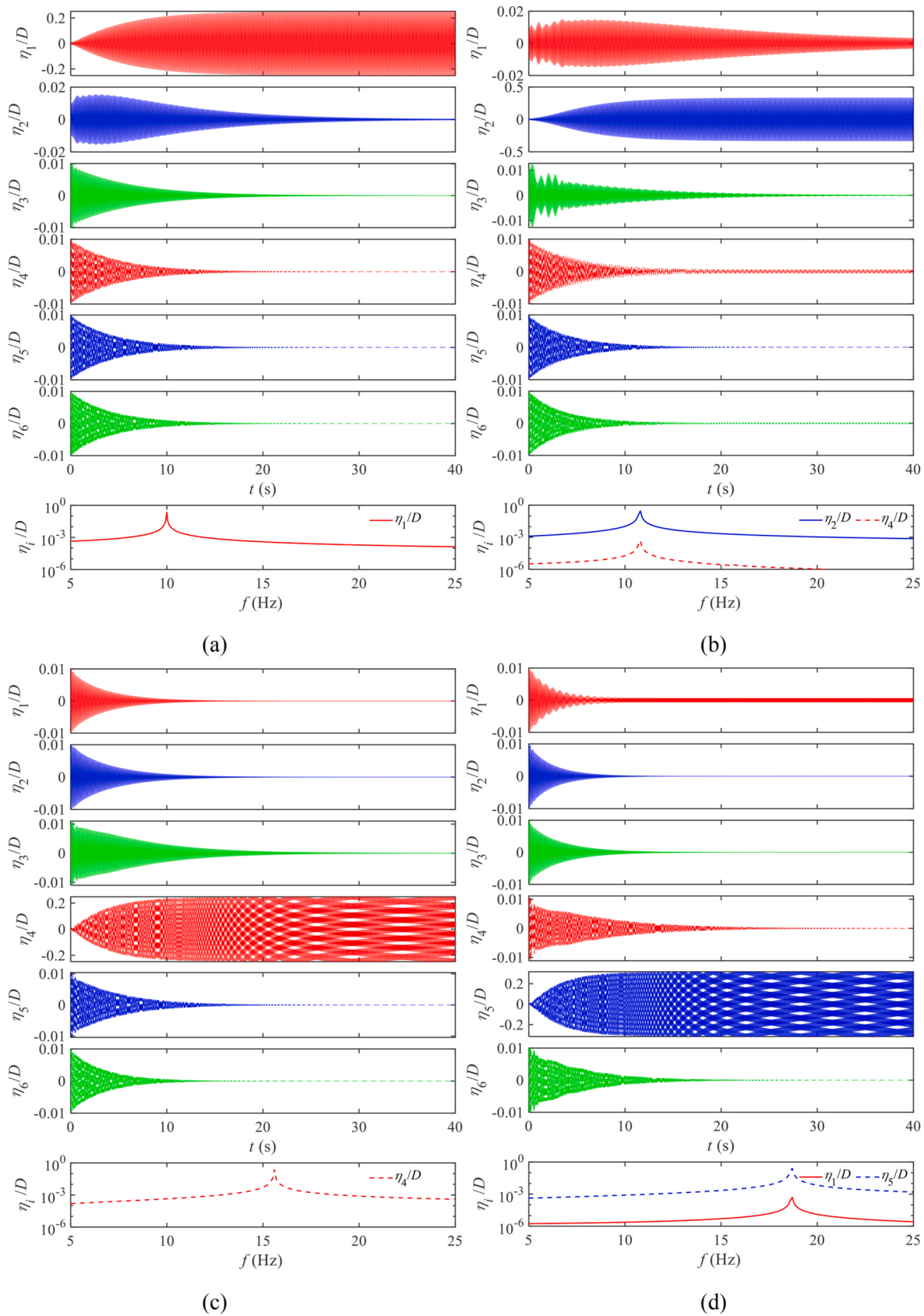


Fig. 5. Time histories and Fourier spectra of displacement responses of the uncontrolled cylinder at various reduced flow velocities: (a) $U/(f_1 D) = 5.0$; (b) $U/(f_1 D) = 5.8$; (c) $U/(f_1 D) = 7.7$; and (d) $U/(f_1 D) = 9.2$.

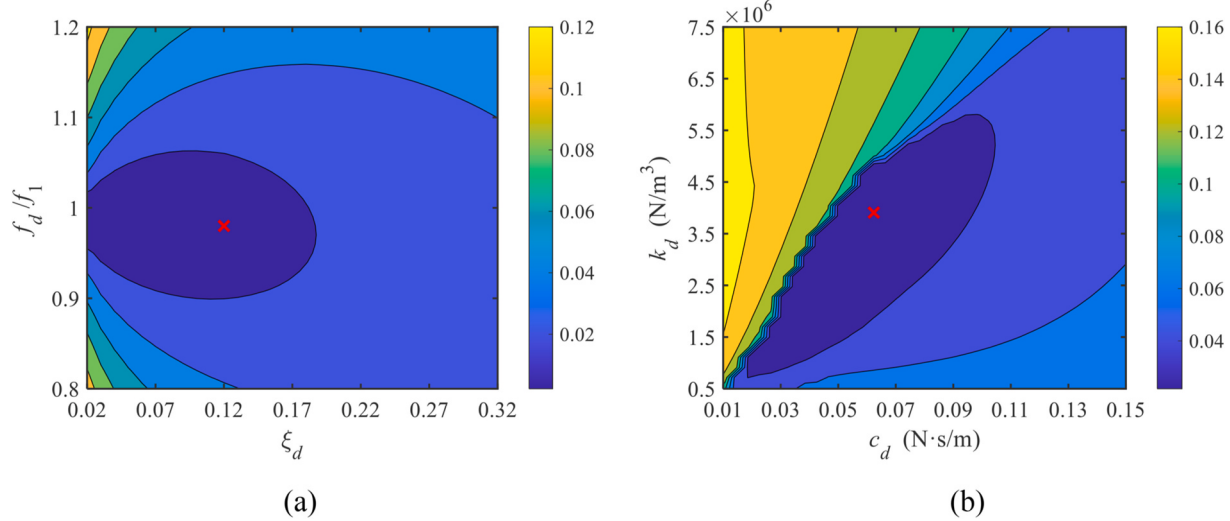


Fig. 6. Steady-state RMS displacements of cylinder-damper systems with $R_m = 0.008$ and various damper stiffness and damping properties at $U/(f_1 D) = 5.0$: (a) cylinder RMS displacements for cylinder-TMD systems; and (b) cylinder RMS displacements for cylinder-NES systems.

No design formula is currently available for NES optimization in VIV control. Although there are some design formulas for TMD optimization in self-excited vibration control (Fujino and Abé, 1993; Chen and Kareem, 2003; Zhang and Xu, 2022), they are targeted to either minimize the vibration amplitude or maximize the critical flow velocity (e.g., for galloping instability). A TMD designed based on these formulas lacks robustness, e.g., to changes in the stiffness of the primary structure (Dai et al., 2020). To design dampers that are both effective and robust, a parametric analysis is conducted to obtain the stiffness coefficients and damping coefficients. Specifically, the equations of motion [i.e., Eq. (8) and Eq. (10)] for fluid-cylinder-damper systems with various damper stiffness and damping coefficients are numerically integrated to obtain their VIV responses. A single-mode analysis is sufficient for TMD design (Fujino and Yoshida, 2002; Dai et al., 2019) since a TMD is targeted for VIV control of a single mode. Both dampers are initially designed to achieve effective and robust controls for the 1st-mode VIV to make a fair comparison. The parametric analysis is conducted at a reduced velocity of $U/(f_1 D) = 5.0$ with the initial conditions of $\eta_1(0) = 0.01D$, $y_d(0) = 0$, $\dot{\eta}_1(0) = 0$, and $\dot{y}_d(0) = 0$. Fig. 6 shows the contour plots of the steady-state RMS displacements of cylinder-damper systems with various damper stiffness and damping properties. Following some previous studies (e.g., Chen and Kareem, 2003; Dai et al., 2020), the stiffness coefficient of the TMD is provided as a frequency ratio f_d/f_1 , and the damping coefficient of the TMD is provided as a damping ratio $\xi_d = c_d/(4\pi m_d f_d)$, where $f_d = \sqrt{k_d/m_d}/2\pi$ is the natural frequency (in Hz) of the TMD. The stiffness and damping coefficients of the TMD are $k_d = m_d(2\pi f_d)^2$ (N/m) and $c_d = 4\pi m_d f_d \xi_d$ (N·s/m), respectively. It is noted that the stiffness coefficients of the TMD and NES have different units.

As seen in Fig. 6(a), the TMD is effective if its natural frequency is close to the target structural natural frequency. The range of frequency ratio f_d/f_1 within which the cylinder amplitude is lower than $0.04D$ achieves the largest value around $\xi_d = 0.12$. Hence, considering both control effectiveness and robustness, the stiffness and damping parameters of the TMD with $R_m = 0.8\%$ are selected as $f_d/f_1 = 0.98$ and $\xi_d = 0.12$, respectively. Fig. 6(b) shows that the effect of the NES depends significantly on its stiffness and damping parameters. To achieve effective and robust VIV control, the NES damping and stiffness properties are selected from the central part of the dark region in Fig. 6(b), i.e., $k_d = 3.91 \times 10^6$ N/m³ and $c_d = 0.0624$ N·s/m, respectively. Red cross markers in Fig. 6 highlight the selected damper properties.

Fig. 7 shows the steady-state RMS displacements of cylinder-damper systems with the designed stiffness and damping properties. The

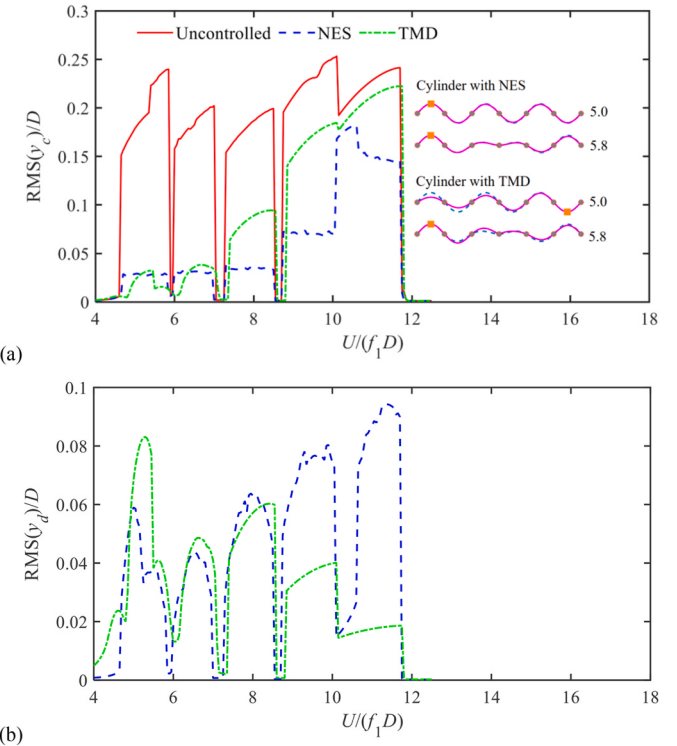


Fig. 7. Steady-state RMS displacements of cylinder-damper systems with $R_m = 0.008$ and designed stiffness and damping properties (the damper is placed at $z = 0.5$ m): (a) cylinder RMS displacements; (b) damper RMS displacements (note: the magenta lines represent the RMS displacements along the cylinder length, and the dashed light-blue lines represent the mode shapes; the circles represent the supporting points, and the squares indicate the locations with the largest RMS displacements). (For interpretation of the references to colour in this figure legend, the reader is referred to the Web version of this article.)

presented RMS displacements are the values of the locations with the largest displacements along the flexible cylinder. The TMD tuned to Mode 1 is capable of effectively suppressing the 1st-mode and 2nd-mode VIVs. This is because the natural frequencies of Mode 1 and Mode 2 are very close (see Table 1) and the modal displacements at the damper location are large, i.e., $\varphi_1(z_d = 0.5) = 1.0$ and $\varphi_2(z_d = 0.5) = 0.9994$,

respectively. The TMD also presents a considerable control effect for the 3rd-mode VIV. The TMD has insignificant control effects for VIVs of higher modes due to the detuning between the natural frequencies of the TMD and main structure. On the other hand, the NES effectively suppresses the 1st-mode, 2nd-mode, 3rd-mode, and 4th-mode VIVs due to its broadband vibration absorption capability. The reduction ratios in these lock-in ranges are higher than 80%. The reduction ratios are higher than the values reported in Dai et al. (2017) with much larger NES mass ratios, in which an elastically mounted rigid cylinder was considered, and the vortex-induced force was simulated using the same wake oscillator model. This was because the NES stiffness and damping properties were not optimized in Dai et al. (2017). The comparison suggests that previous studies may have underestimated the effectiveness of an NES because the NES parameters were chosen without a systematic design.

The NES also presents a considerable control effect for the 5th-mode VIV, while the NES has an insignificant control effect for the 6th-mode VIV. The reduced control effect of the NES for the 5th-mode and 6th-mode VIVs is mainly because the modal displacements at the damper location are small, i.e., $\varphi_5(z_d = 0.5) = 0.50$ and $\varphi_6(z_d = 0.5) = 0.27$, respectively. The 6th-mode VIV can be effectively suppressed if the NES is moved to the midspan of the 3rd span, where the modal displacement of Mode 6 is large. This is confirmed in Fig. 8, which shows the steady-state RMS displacements of cylinder-damper systems with the same cylinder and damper properties except that the damper is moved to $z = 2.5$ m. The 6th-mode VIV is effectively suppressed by the NES as expected. The control effect of the TMD is also remarkably increased for the 6th-mode VIV, while the controlled response is still large because of the detuning between the TMD frequency and mode natural frequency. On the other hand, the suppression effect for the 2nd-mode VIV is reduced for both dampers because the modal displacement of Mode 2 is very small at the new damper location, i.e., $\varphi_2(z_d = 2.5) = 0.27$. The control effects for other modes remain almost unchanged in Figs. 7 and 8 since the modal displacements of these modes are very close at $z = 0.5$ and 2.5 m. The results in Figs. 7 and 8 prove that the designed NES can effectively control the VIVs of multiple modes, providing that the modal displacements at the NES location are not too small. Compared to the NES, the TMD is more effective at most reduced velocities in the lock-in range of Mode 1. However, the NES is more effective than the TMD for higher-order mode VIV controls. The increased effectiveness of the NES for VIV controls of multiple modes also suggests that the NES is more robust than the TMD to changes in the frequencies of the primary structure. Hence, the NES can serve as a competitive choice for VIV

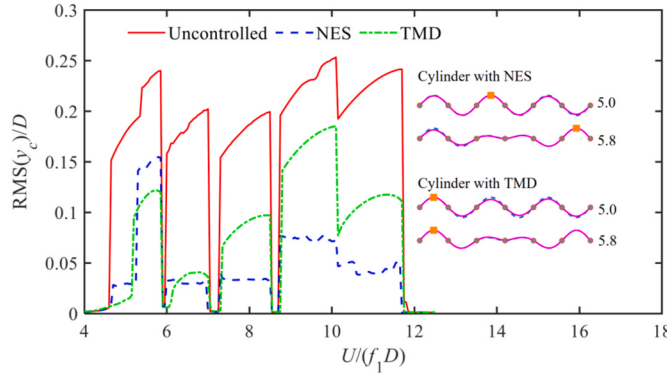


Fig. 8. Steady-state cylinder RMS displacements of cylinder-damper systems with $R_m = 0.008$ and optimized stiffness and damping properties (note: the damper is placed at $z = 2.5$ m; the magenta lines represent the RMS displacements along the cylinder length, and the dashed light-blue lines represent the mode shapes; the circles represent the supporting points, and the squares indicate the locations with the largest RMS displacements). (For interpretation of the references to colour in this figure legend, the reader is referred to the Web version of this article.)

control of multiple-degree-of-freedom flexible structures.

The magenta lines in Figs. 7(a) and 8 show the RMS displacements along the cylinder length at $U/(f_1 D) = 5.0$ and 5.8. These two reduced velocities lie within the lock-in ranges of Mode 1 and Mode 2 for the uncontrolled cylinder. Hence, the mode shapes of these two modes are also presented (dashed light-blue lines) for comparison. Since the VIV response contains secondary components from several other modes (which is discussed later), the RMS displacements along the cylinder do not precisely follow the mode shape of the dominant mode. In addition, the maximum displacements at various z locations may not be achieved simultaneously. The VIV responses in the lock-in ranges of Modes 3, 4, 5, and 6 almost exactly follow their respective mode shapes, and hence, the RMS displacements along the cylinder length are not shown.

Fig. 7(b) show that the RMS displacements of the NES are of the same order as the RMS displacements of the TMD. The maximum RMS displacements of the NES and TMD are $0.105D$ and $0.096D$, respectively, if the dampers are placed at $z = 2.5$ m. The maximum RMS displacements of the NES and TMD are slightly smaller if the dampers are placed at $z = 0.5$ m. Hence, the designed dampers can be implemented inside the circular cylinder without colliding with the cylinder surface.

The time histories and Fourier spectra of typical displacement responses of the cylinder-TMD system are presented in Fig. 9. The Fourier spectra are calculated based on the steady-state displacement signals. The time histories and Fourier spectra show that the displacements of the cylinder-TMD system are quasi-harmonic signals dominated by a single frequency. The TMD resonates with the circular cylinder, which is equivalent to an increase in the effective damping ratio of the circular cylinder and hence results in a reduced VIV response compared to the uncontrolled cylinder (Dai et al., 2020). The steady-state VIV response of the circular cylinder at each reduced velocity consists of not only the vibration of a dominant mode but also secondary components from several other modes. The frequencies of the secondary components are consistent with the frequency of the dominant component. This is because the vortex shedding and TMD vibration are synchronized to the vibration of the dominant mode; hence, the vibrations of the secondary components are forced vibrations following the frequency of the dominant mode. As discussed earlier, the strength of coupling between two modes (e.g., Mode k and Mode n) due to aeroelastic nonlinearity is determined by the quantity of $\int_0^L \varphi_n^3(z) \varphi_k(z) dz / \int_0^L \varphi_k^2(z) dz$, which is not significant according to Figs. 4 and 5. If the VIV response is dominated by Mode n , the effect of TMD attachment on Mode k is similar to a harmonic force $k_d[\varphi_n(z_d)\eta_n(t) - y_d(t)]\varphi_k(z_d)$, as seen from Eq. (10a). As a result, significant coupling exists between Mode 1 and Mode 2 due to their very close natural frequencies and the large values of $\varphi_1(z_d = 0.5)$ and $\varphi_2(z_d = 0.5)$, as shown by the responses at $U/(f_1 D) = 5.0$ and 5.8 [Fig. 9(a) and (b)]. The multimode coupling effects at higher reduced velocities are insignificant due to the increased frequency deviations (between the dominant and coupling modes) and/or the reduced values of $\varphi_n(z_d = 0.5)$ ($n = 5, 6$), as shown in Fig. 9(c) and (d).

The time histories and Fourier spectra of typical displacement responses of the cylinder-NES system are presented in Fig. 10. The Fourier spectra are calculated based on the steady-state displacement signals. The cylinder-NES system exhibits a strongly modulated response (Lee et al., 2008; Tumkur et al., 2013b). Gendelman et al. (2010) showed that the strongly modulated response occurs if there is no attractor in the form of a stable equilibrium point on the slow invariant manifold of the coupled system of the primary oscillator and NES. The Fourier spectra show that in the lock-in range for a specific mode, the displacements of the circular cylinder and NES have the largest components at the natural frequency of this specific mode, which indicates a 1:1 resonance capture between the cylinder and NES. The displacements include multiple frequency components due to the essentially nonlinear nature of the NES stiffness. Resonance capture cascades may exist at the transient stage, but this is not further analysed in this study. As seen from Eq. (8a), if the

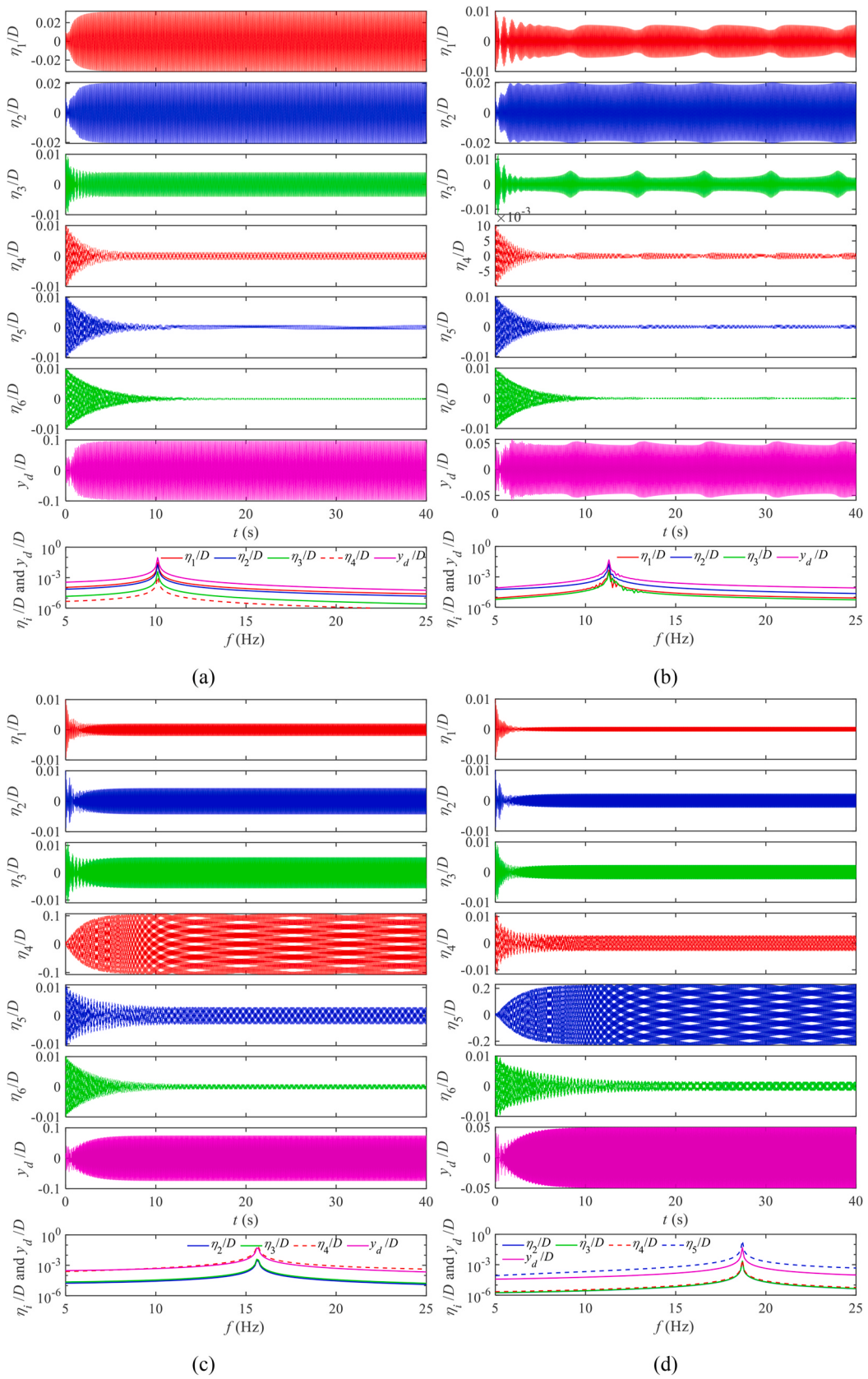


Fig. 9. Time histories and Fourier spectra of displacement responses of the cylinder-TMD system at various reduced flow velocities: (a) $U/(f_1 D) = 5.0$; (b) $U/(f_1 D) = 5.8$; (c) $U/(f_1 D) = 7.7$; and (d) $U/(f_1 D) = 9.2$.

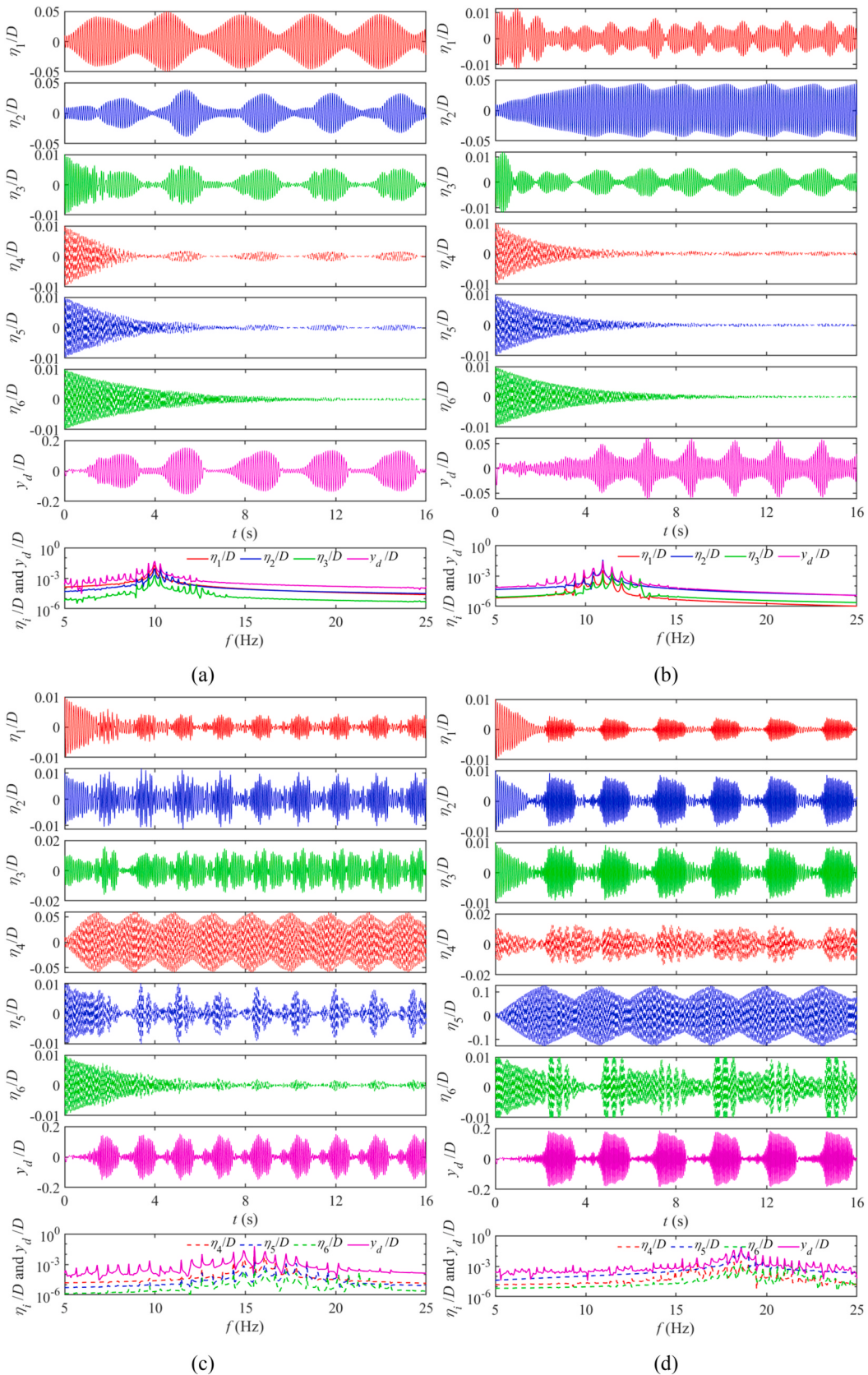


Fig. 10. Time histories and Fourier spectra of displacement responses of the cylinder-NES system at various reduced flow velocities: (a) $U/(f_1 D) = 5.0$; (b) $U/(f_1 D) = 5.8$; (c) $U/(f_1 D) = 7.7$; and (d) $U/(f_1 D) = 9.2$.

VIV response is dominated by Mode n , the effects of the NES on the secondary modes are similar to external forces $k_d[\varphi_n(z_d)\eta_n(t) - y_d(t)]^3\varphi_k(z_d)$, which have the largest components at the natural frequency of Mode n . Hence, similar to the response of the cylinder-TMD system, significant coupling exists for the cylinder-NES system between Mode 1 and Mode 2 due to their very close natural frequencies, as shown in Fig. 10(a) and (b). The multimode coupling effects at higher reduced velocities are insignificant, as shown in Fig. 10(c) and (d).

The large-amplitude VIVs of an uncontrolled circular cylinder and a cylinder-TMD system in low-turbulent flows are often quasi-harmonic vibrations, as confirmed in Figs. 5 and 9. For a harmonic or a quasi-harmonic vibration, the maximum displacement is approximately $\sqrt{2}$ times the RMS displacement. Due to the straightforward relationship between RMS displacement and maximum displacement, it is often specified in structural designs that the RMS displacements of VIVs should be lower than a threshold value (e.g., Pettigrew and Taylor, 2003). However, the maximum displacement of a strongly modulated response can be much larger than $\sqrt{2}$ times the RMS displacement. For example, the RMS displacement of the NES at $U/(f_1 D) = 7.7$ is 0.057 D , while the maximum displacement is 0.15 D . Hence, for a cylinder-NES system, it might be necessary to specify threshold values for both RMS displacement and maximum displacement.

3.4. Robustness of the NES performance to the stiffness and damping properties of the cylinder and NES

In addition to the control effectiveness, another important issue in VIV control is to ensure the robustness of the control measure to various uncertainties. For example, the natural frequency and damping ratio of the circular cylinder may change due to structural degradation. Additionally, the stiffness and damping properties of a practically used damper may not be exactly the same as the designed damper due to

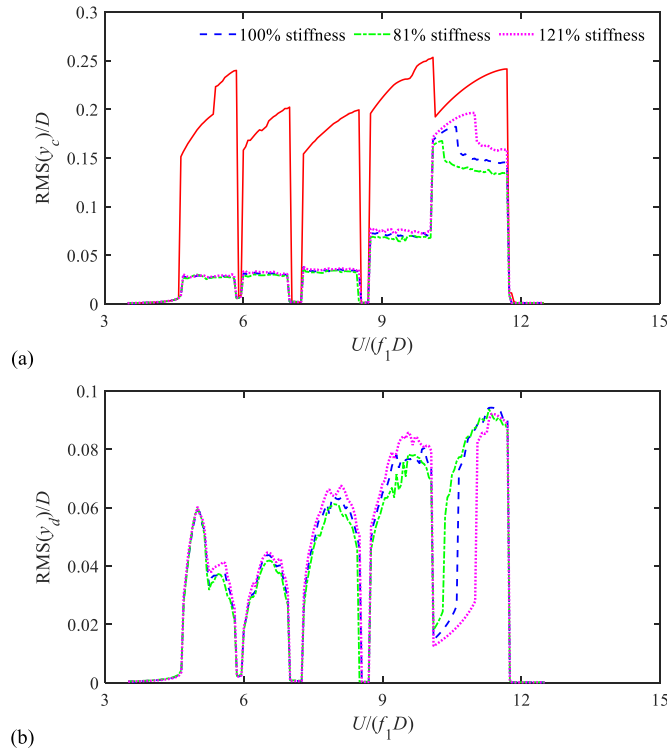


Fig. 11. Steady-state RMS displacements of cylinder-NES systems with $R_m = 0.008$ and various bridge stiffness properties: (a) cylinder RMS displacements; and (b) damper RMS displacements.

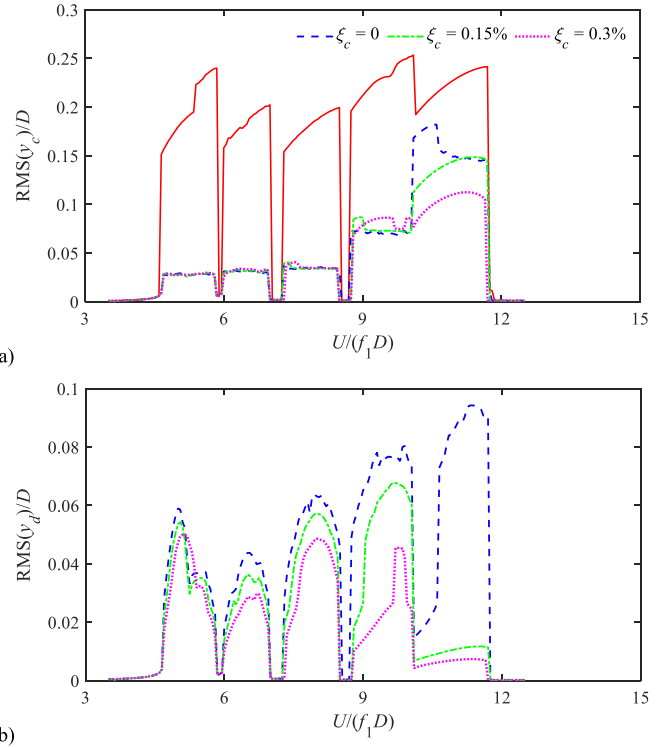


Fig. 12. Steady-state RMS displacements of cylinder-NES systems with $R_m = 0.008$ and various bridge damping properties: (a) cylinder RMS displacements; and (b) damper RMS displacements.

underlying design and fabrication errors. It is thus necessary to ensure that the control measure is robust to these uncertainties before the measure can be considered reliable for practical application. Hence, the robustness of the NES performance to the uncertainties of the stiffness and damping properties of the circular cylinder and damper is investigated in this subsection. Throughout this subsection, a six-mode approximation is adopted, and the NES mass ratio is $m_d/(m_L) = 0.80\%$.

Fig. 11 shows the steady-state RMS displacements of the cylinder-NES systems when the stiffness of the circular cylinder is decreased by 19% and increased by 21%. These stiffness variations correspond to a 10% decrease and a 10% increase in the cylinder natural frequencies, respectively. As seen from the figure, the variation in the cylinder stiffness exhibits insignificant changes to the vibration responses of the cylinder-NES system in the lock-in ranges of the first 5 modes. This is expected since the NES can absorb broadband vibration energy from the primary structure. The effect of the stiffness variation of the circular cylinder on the vibration responses is more visible in the lock-in range of Mode 6. More specifically, the cylinder response is slightly increased, while the NES response is decreased by increasing the cylinder stiffness. The results in Fig. 11 confirm that the performance of an NES is robust to the uncertainty of the stiffness of the primary structure.

Fig. 12 shows the steady-state RMS displacements of cylinder-NES systems with various cylinder damping properties. It is noted that the NES designed for $\xi_c = 0$ is also effective for other cylinder damping properties, i.e., $\xi_c = 0.15\%$ and 0.30% . Specifically, the vibration response of the circular cylinder is insignificantly affected, while the response of the NES is decreased by increasing the cylinder damping ratio. This is because the NES becomes ineffective if the vibration amplitude of the primary structure becomes very low or very high. Indeed, due to the amplitude dependency of the NES stiffness, the NES is only effective for a specific range of vibration amplitudes within which the NES can resonate with the primary structure (Lee et al., 2008; Tumkur et al., 2013a; Wang et al., 2015). As a result, once the NES can reduce the VIV amplitude to a very low level, a further increase in the

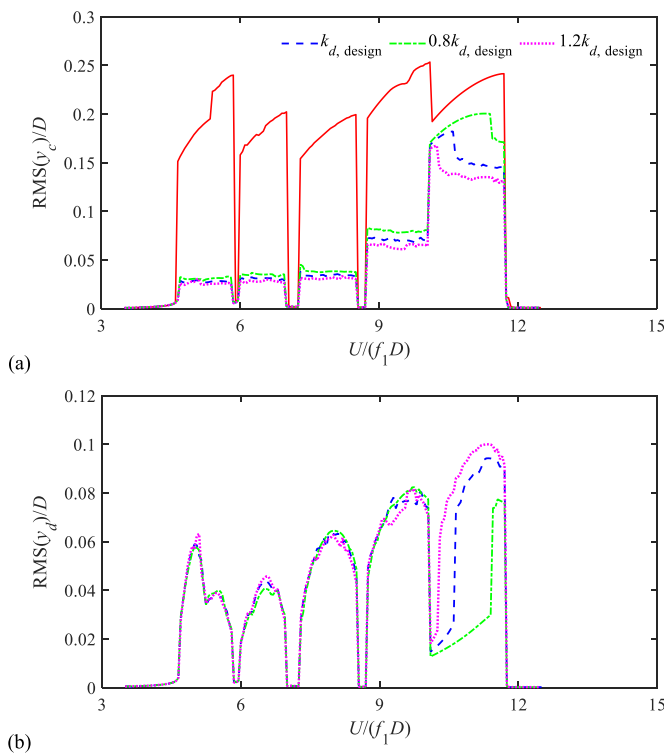


Fig. 13. Steady-state RMS displacements of cylinder-NES systems with $R_m = 0.008$ and various NES stiffness properties: (a) cylinder RMS displacements; and (b) damper RMS displacements.

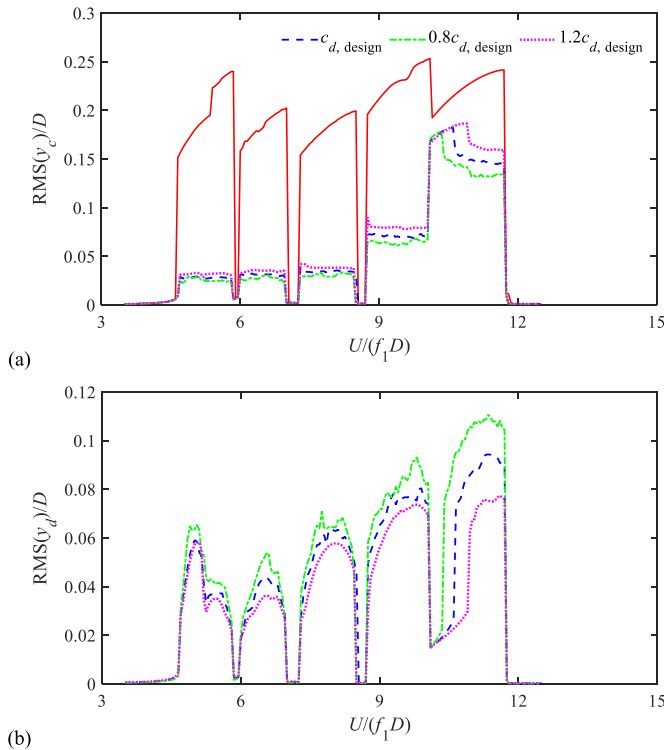


Fig. 14. Steady-state RMS displacements of cylinder-NES systems with $R_m = 0.008$ and various NES damping properties: (a) cylinder RMS displacements; and (b) damper RMS displacements.

cylinder damping ratio cannot significantly reduce the VIV amplitude, as shown in Fig. 12(a). The vibration response of the NES decreases since less energy is dissipated by the NES with increasing cylinder damping ratio.

Fig. 13 shows the steady-state RMS displacements of cylinder-NES systems with various NES stiffness properties. The effect of increasing the NES stiffness is similar to the effect of decreasing the cylinder stiffness: (i) the variation of the NES stiffness exhibits insignificant changes to the vibration responses of the cylinder-NES system in the lock-in ranges of the first 5 modes; and (ii) the cylinder response is slightly increased while the NES response is decreased by decreasing the NES stiffness in the lock-in range of Mode 6. Overall, the performance of the NES is very robust to changes in the NES stiffness.

Fig. 14 shows the steady-state RMS displacements of cylinder-NES systems with various NES-damping properties. As seen from the figure, an increase in the NES-damping results in an insignificantly increased vibration response of the cylinder and a decreased response of the NES. The results show that the performance of an NES is robust to the uncertainty of the damping property of the NES.

In summary, the performance of the NES is robust to uncertainties in the stiffness and damping properties of the primary structure and the NES. These features make the NES a competitive choice for robust VIV control of various flexible structures.

4. Further discussion

After showing that the NES is effective and robust for controlling the VIV of the flexible circular cylinder, some further discussion, including the effect of NES mass on the control performance and the applicability of the single-mode approximation for the cylinder-NES system, is examined in this section.

4.1. Effect of NES mass

It is expected that both the effectiveness and robustness of a damper can be enhanced by increasing the mass ratio $m_d/(m_c L)$. To study the effect of the damper mass ratio, the stiffness and damping properties of NESs with $R_m = 0.4\%$, 1.2% , and 1.5% are designed through similar parametric analyses as those shown in Fig. 6. The contour plots for cylinder-NES systems with various mass ratios are not shown for brevity. The designed stiffness and damping properties for the NESs with different mass ratios are listed in Table 2. As seen from the table, both the designed stiffness and damping properties for the NES increase with increasing mass ratio. Fig. 15 presents the steady-state RMS displacements of cylinder-NES systems with various mass ratios and dynamic properties provided in Table 2. It is noted that the vibration responses of the cylinder-NES system decrease remarkably with increasing mass ratio.

As mentioned in the Introduction, Mehmod et al. (2014) discussed the effect of the NES mass ratio $m_d/(m_c L)$ on the VIV control of an elastically mounted rigid circular cylinder based on computational fluid dynamic simulations. They stated that the NES mass ratio $m_d/(m_c L)$ should be larger than a critical value to achieve effective VIV control. However, the NES stiffness and damping properties in the study by Mehmod et al. (2014) were chosen without a systematic design. Indeed, they considered constant stiffness and damping properties for NESs with various mass ratios. Fig. 16 shows the minimum cylinder RMS

Table 2
Optimal stiffness and damping properties of NESs with various mass ratios.

Mass ratio	Stiffness coefficient (N/m^3)	Damping coefficient ($\text{N}\cdot\text{s}/\text{m}$)
0.4%	7.56×10^5	0.0305
0.8%	3.91×10^6	0.0624
1.2%	1.41×10^7	0.1154
1.5%	5.25×10^7	0.3094

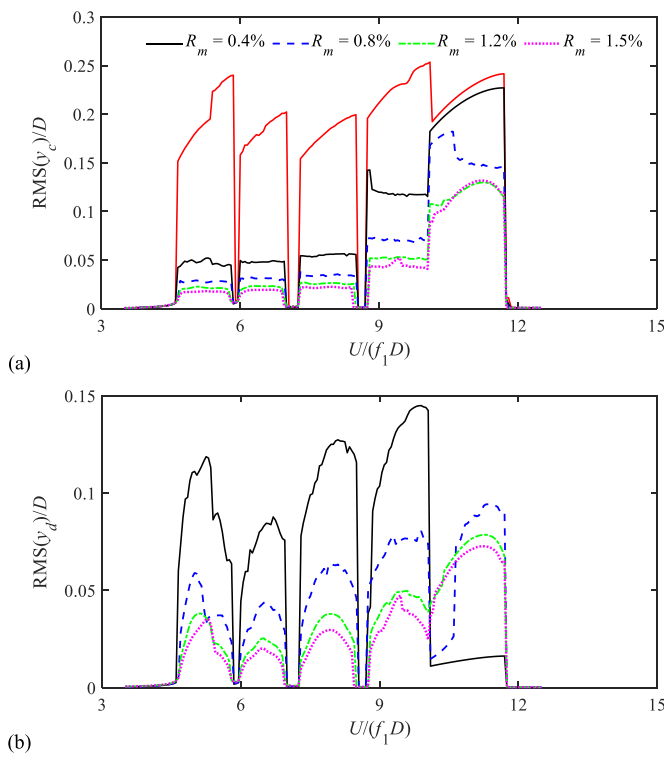


Fig. 15. Steady-state RMS displacements of cylinder-NES systems with various mass ratios: (a) cylinder RMS displacements; and (b) damper RMS displacements.

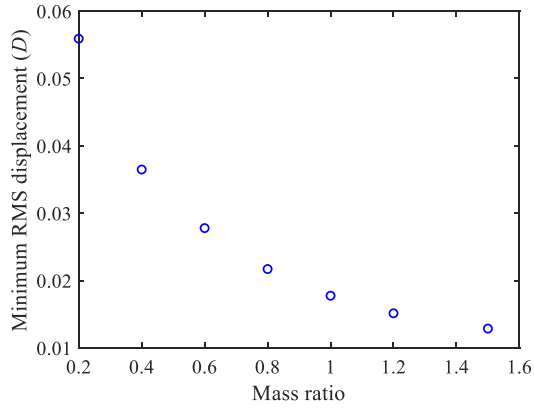


Fig. 16. Minimum cylinder RMS displacements achieved by NESs with various mass ratios.

displacements of the present cylinder-NES system at $U/(f_1 D) = 5.0$ achieved by NESs with various mass ratios. The minimum cylinder RMS displacement for a specific mass ratio is obtained by a parametric analysis in which the responses of cylinder-NES systems with various NES stiffness and damping properties are calculated. Unlike the results reported by Mehmod et al. (2014) which exhibited a sharp reduction in the cylinder response between $m_d/(m_c L) = 2.0\%$ and 3.0% , the minimum cylinder RMS displacement in Fig. 16 decreases continuously with increasing NES mass ratio. The decreasing rate of the cylinder RMS displacement in Fig. 16 becomes slower with increasing mass ratio. The results in Fig. 16 suggest that although the NES stiffness and damping properties can be optimized to enhance the control effectiveness, a critical mass ratio of the NES is still required if it is to ensure that the vibration response of the primary structure is lower than a threshold value.

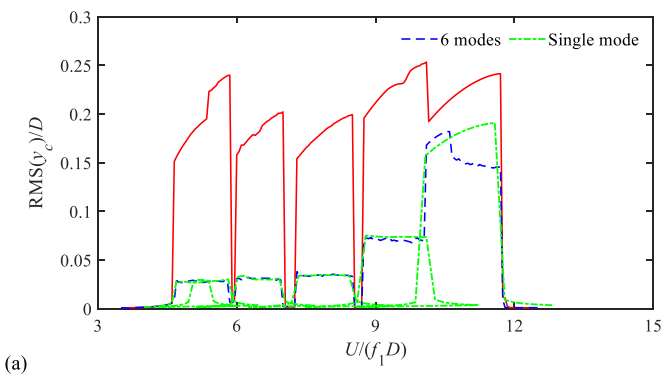


Fig. 17. Steady-state RMS displacements of the cylinder-NES system by the single-mode approximation and 6-mode approximation (the damper is placed at $z = 0.5$ m): (a) cylinder RMS displacements; and (b) damper RMS displacements.

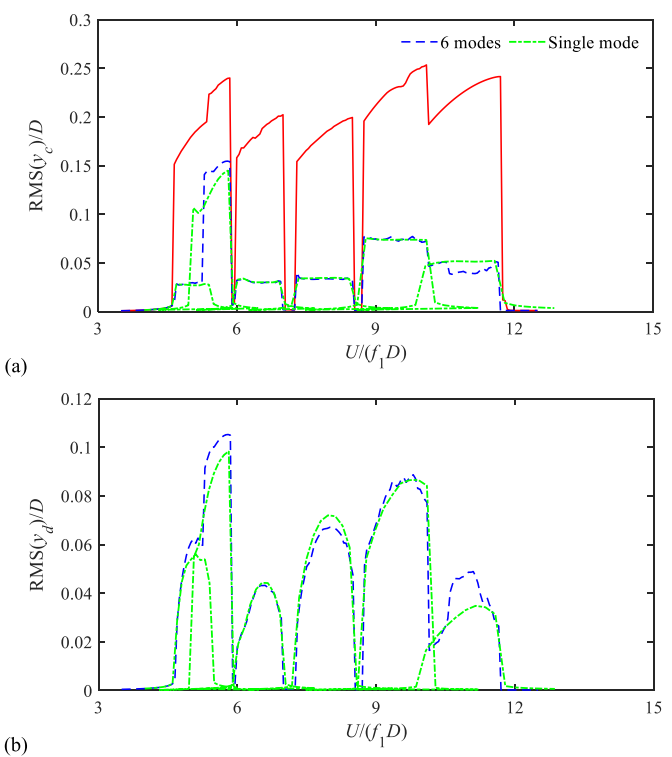


Fig. 18. Steady-state RMS displacements of the cylinder-NES system by the single-mode approximation and 6-mode approximation (the damper is placed at $z = 2.5$ m): (a) cylinder RMS displacements; and (b) damper RMS displacements.

4.2. Applicability of the single-mode approximation for the cylinder-NES system

For a structure with a large mass ratio (between the structure and displaced fluid) immersed in a uniform flow, aeroelastic model experiments and field measurements suggest that the VIV is often dominated by a single natural mode (e.g., Chen et al., 2015; Lupi et al., 2017). The dominant mode may change with varying flow velocity. Hence, the single-mode approximation is often adopted for the structural displacement in the VIV analysis, which greatly reduces the computational cost. For the uncontrolled cylinder considered in this paper, Fig. 4 shows that the single-mode approximation predicts accurate VIV responses in the lock-in ranges of Modes 1, 3, and 4, while it slightly underestimates the responses in the lock-in ranges of Modes 2, 5, and 6. Due to the coupling term introduced by the NES [i.e., the curly bracketed term on the left-hand side of Eq. (8a)] and the NES's capability to resonate with various modes, it remains unclear if the single-mode approximation is still applicable for the cylinder-NES system. To this end, a mode-by-mode analysis [with $N = 1$ in Eq. (8)] is conducted for the cylinder-NES system. The NES mass ratio is $m_d/(m_c L) = 0.80\%$, and the stiffness and damping properties are highlighted in Fig. 6(c). Fig. 17 compares the steady-state RMS displacements of the cylinder-NES system with the damper placed at $z = 0.5$ m calculated by a single-mode approximation and a six-mode approximation. Fig. 18 presents a similar comparison for the cylinder-NES system with the damper placed at $z = 2.5$ m. The RMS displacements calculated by the single-mode approximation generally agree well with the results calculated by the six-mode approximation for both cylinder-NES systems. This is expected for the lock-in ranges of Modes 3, 4, and 5 since the vibrations of the cylinder-NES system at these reduced velocities are dominated by their respective modes, as demonstrated in Fig. 10(c) and (d).

In the lock-in ranges of Mode 1 and Mode 2, although the RMS displacements of the cylinder-NES systems are reasonably calculated by the single-mode approximation, the response behaviours by the single-mode

approximation and the six-mode approximation are actually quite different. Fig. 10(a) and (b) shows that the vibration responses of the six-mode approximation show remarkable coupling between Mode 1 and Mode 2. The multimode coupling cannot be predicted by the single-mode assumption, as seen in Fig. 19(a) and (b), which shows the vibration responses of the cylinder-NES system (with damper placed at $z = 0.5$ m) calculated by the single-mode approximation at $U/(f_1 D) = 5.0$ and 5.8. In addition, the six-mode approximation results in a strongly modulated response, while the single-mode approximation results in a quasi-harmonic response. As a result, the maximum displacements of the cylinder-NES system may be largely underestimated by the single-mode approximation. As an example, the maximum NES displacements at $U/(f_1 D) = 5.0$ are $0.153D$ by the six-mode approximation and $0.110D$ by the single-mode approximation. As shown in Fig. 10(c and d) and 19 (c, d), both the single-mode approximation and six-mode approximation predict strongly modulated responses at $U/(f_1 D) = 7.7$ and 9.2, and the global response behaviours by the two approximations agree reasonably well. This is expected since the responses at $U/(f_1 D) = 7.7$ or 9.2 are dominated by a single mode. However, the maximum displacements of the NES are largely overestimated by the single-mode approximation. More specifically, the maximum NES displacements calculated by the six-mode approximation are $0.150D$ and $0.184D$, respectively, while the results calculated by the single-mode approximation are $0.180D$ and $0.234D$, respectively. The lower NES response in the six-mode approximation is probably because a portion of kinetic energy in the dominant mode is transferred to other secondary modes (e.g., due to the coupling effect introduced by the NES) and further dissipated by the aeroelastic damping. As discussed earlier, the effects of the NES on the secondary modes are similar to external forces at the frequency of the dominant mode. As a result, less energy is dissipated by the NES in the six-mode approximation than in the single-mode approximation. This examination suggests that the RMS displacements of the cylinder-NES system can be reasonably estimated, while the maximum displacements may be largely overestimated or underestimated by the single-mode approximation.

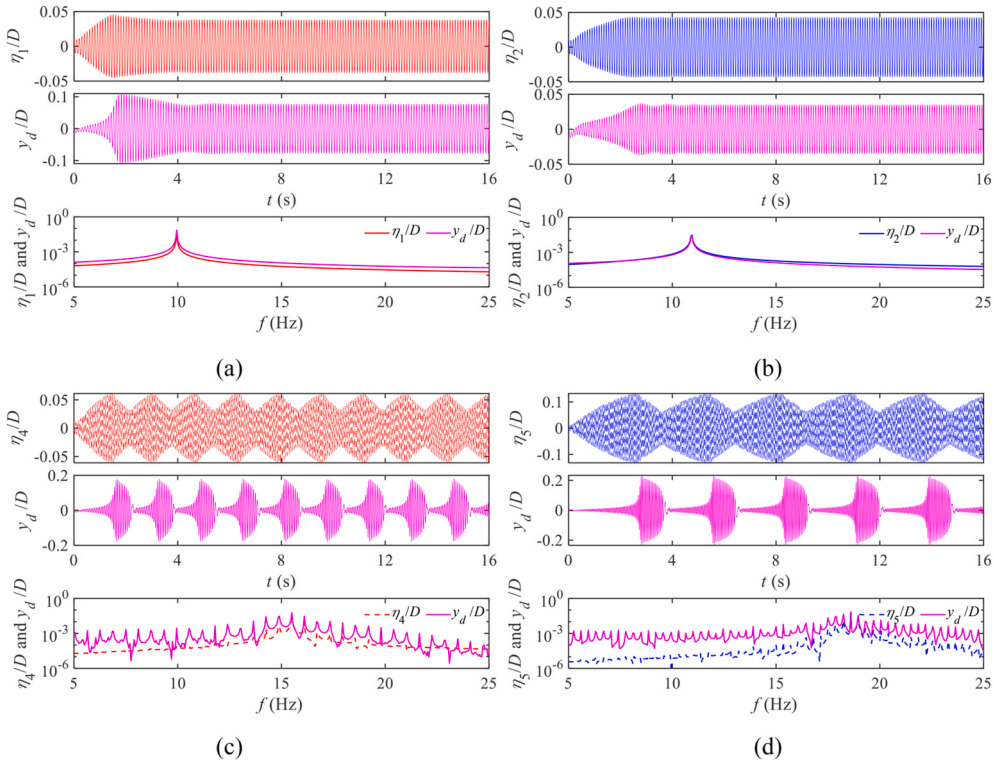


Fig. 19. Time histories and Fourier spectra of displacement responses of cylinder-NES systems (the damper is placed at $z = 0.5$ m) at various reduced flow velocities calculated by single-mode approximation: (a) $U/(f_1 D) = 5.0$; (b) $U/(f_1 D) = 5.8$; (c) $U/(f_1 D) = 7.7$; and (d) $U/(f_1 D) = 9.2$.

5. Concluding remarks

This study numerically examined the vortex-induced vibration (VIV) control of a flexible circular cylinder using a nonlinear energy sink (NES). An example cylinder of a six-span continuous beam was investigated, and the NES was considered as a lumped mass attachment with cubic stiffness and linear damping. The numerical results suggested that an NES designed for VIV control of the fundamental mode can effectively mitigate the VIVs of higher-order modes, providing that the modal displacement at the NES location is not too small. The performance of the NES was robust to uncertainties in the stiffness and damping properties of the primary structure and NES. These features make the NES a competitive choice for effective and robust VIV control of various flexible structures with multiple degrees of freedom. The control effectiveness of an NES can be enhanced by increasing the mass ratio, and the optimal stiffness and damping properties of the NES increase with increasing mass ratio. Since the minimum cylinder response of the cylinder-NES system decreases with increasing NES mass ratio, a critical mass ratio of the NES may be required if the control target is to ensure that the vibration response of the primary structure is lower than a threshold value. It was also revealed that the root-mean-square (RMS) displacements of the cylinder-NES system can be reasonably estimated by the single-mode approximation of the cylinder displacement, while the maximum displacements may be largely overestimated or underestimated. Finally, it should be noted that this study is limited to numerical simulations while experimental investigations should be conducted to further validate the applicability of NES for VIV control.

CRediT authorship contribution statement

Mingjie Zhang: Conceptualization, Methodology, Software, Formal analysis, Investigation, Data curation, Writing – original draft, Writing – original draft, Writing – review & editing. **Teng Wu:** Conceptualization, Methodology, Investigation, Writing – original draft, Writing – review & editing. **Ole Øiseth:** Methodology, Investigation, Writing – original draft, Writing – review & editing, Funding acquisition.

Declaration of competing interest

The authors declare that they have no known competing financial interests or personal relationships that could have appeared to influence the work reported in this paper.

Data availability

Data will be made available on request.

Acknowledgments

The authors gratefully acknowledge the support of their partners Equinor Energy AS, ConocoPhillips Skandinavia AS, NTNU, SINTEF, and the Research Council of Norway (strategic Norwegian research program PETROMAKS2, grant agreement number 280713).

References

- Benidir, A., Flamand, O., Gaillet, L., Dimitriadis, G., 2015. Impact of roughness and circularity-defect on bridge cables stability. *J. Wind Eng. Ind. Aerod.* 137, 1–13.
- Cantero, D., Øiseth, O., Rønquist, A., 2018. Indirect monitoring of vortex-induced vibration of suspension bridge hangers. *Struct. Health Monit.* 17 (4), 837–849.
- Chen, D., Gu, C., Fang, K., Yang, J., Guo, D., Marzocca, P., 2021. Vortex-induced vibration of a cylinder with nonlinear energy sink (NES) at low Reynolds number. *Nonlinear Dynam.* 104 (3), 1937–1954.
- Chen, D., Marzocca, P., Xiao, Q., Zhan, Z., Gu, C., 2020. Vortex-induced vibration on a low mass ratio cylinder with a nonlinear dissipative oscillator at moderate Reynolds number. *J. Fluid Struct.* 99, 103160.
- Chen, W.L., Zhang, Q.Q., Li, H., Hu, H., 2015. An experimental investigation on vortex induced vibration of a flexible inclined cable under a shear flow. *J. Fluid Struct.* 54, 297–311.
- Chen, X., Kareem, A., 2003. Efficacy of tuned mass dampers for bridge flutter control. *J. Struct. Eng.* 129 (10), 1291–1300.
- Dai, H.L., Abdelkefi, A., Wang, L., 2017. Vortex-induced vibrations mitigation through a nonlinear energy sink. *Commun. Nonlinear Sci. Numer. Simulat.* 42, 22–36.
- Dai, J., Xu, Z.D., Gai, P.P., 2019. Tuned mass-damper-inerter control of wind-induced vibration of flexible structures based on inerter location. *Eng. Struct.* 199, 109585.
- Dai, J., Xu, Z.D., Gai, P.P., 2020. Parameter determination of the tuned mass damper mitigating the vortex-induced vibration in bridges. *Eng. Struct.* 221, 111084.
- Demartino, C., Ricciardelli, F., 2017. Aerodynamics of nominally circular cylinders: a review of experimental results for Civil Engineering applications. *Eng. Struct.* 137, 76–114.
- Demartino, C., Ricciardelli, F., 2018. Assessment of the structural damping required to prevent galloping of dry HDPE stay cables using the quasi-steady approach. *J. Bridge Eng.* 23 (4), 04018004.
- Facchinetti, M.L., De Langre, E., Biolley, F., 2004. Coupling of structure and wake oscillators in vortex-induced vibrations. *J. Fluid Struct.* 19 (2), 123–140.
- Fujino, Y., Abé, M., 1993. Design formulas for tuned mass dampers based on a perturbation technique. *Earthq. Eng. Struct. Dynam.* 22 (10), 833–854.
- Fujino, Y., Yoshida, Y., 2002. Wind-induced vibration and control of Trans-Tokyo Bay crossing bridge. *J. Struct. Eng.* 128 (8), 1012–1025.
- Gabbai, R., Benaroya, H., 2005. An overview of modeling and experiments of vortex-induced vibration of circular cylinders. *J. Sound Vib.* 282, 575–616.
- Gendelman, O., Manevitch, L.I., Vakakis, A.F., McClosey, R., 2001. Energy pumping in nonlinear mechanical oscillators: part I—dynamics of the underlying Hamiltonian systems. *J. Appl. Mech.* 68 (1), 34–41.
- Gendelman, O.V., Vakakis, A.F., Bergman, L.A., McFarland, D.M., 2010. Asymptotic analysis of passive nonlinear suppression of aeroelastic instabilities of a rigid wing in subsonic flow. *SIAM J. Appl. Math.* 70 (5), 1655–1677.
- Hasheminejad, S.M., Rabieh, A.H., Markazi, A.H.D., 2018. Dual-functional electromagnetic energy harvesting and vortex-induced vibration control of an elastically mounted circular cylinder. *J. Eng. Mech.* 144 (3), 04017184.
- Ishihara, T., Li, T., 2020. Numerical study on suppression of vortex-induced vibration of circular cylinder by helical wires. *J. Wind Eng. Ind. Aerod.* 197, 104081.
- Keber, M., Wiercigroch, M., 2008. Dynamics of a vertical riser with weak structural nonlinearity excited by wakes. *J. Sound Vib.* 315 (3), 685–699.
- Kerschen, G., Kowtko, J.J., McFarland, D.M., Bergman, L.A., Vakakis, A.F., 2007. Theoretical and experimental study of multimodal targeted energy transfer in a system of coupled oscillators. *Nonlinear Dynam.* 47 (1), 285–309.
- Kerschen, G., Lee, Y.S., Vakakis, A.F., McFarland, D.M., Bergman, L.A., 2005. Irreversible passive energy transfer in coupled oscillators with essential nonlinearity. *SIAM J. Appl. Math.* 66 (2), 648–679.
- Krenk, S., 2009. Non-linear Modeling and Analysis of Solids and Structures. Cambridge University Press.
- Le Diouron, T., Fujino, Y., Abe, M., 2003. Control of wind-induced self-excited oscillations by transfer of internal energy to higher modes of vibration. II: application to taut cables. *J. Eng. Mech.* 129 (5), 526–538.
- Lee, Y.S., Kerschen, G., Vakakis, A.F., Panagopoulos, P., Bergman, L., McFarland, D.M., 2005. Complicated dynamics of a linear oscillator with a light, essentially nonlinear attachment. *Phys. Nonlinear Phenom.* 204 (1–2), 41–69.
- Lee, Y.S., Vakakis, A.F., Bergman, L.A., McFarland, D.M., Kerschen, G., 2008. Enhancing the robustness of aeroelastic instability suppression using multi-degree-of-freedom nonlinear energy sinks. *AIAA J.* 46 (6), 1371–1394.
- Lupi, F., Niemann, H.J., Höffer, R., 2017. A novel spectral method for cross-wind vibrations: application to 27 full-scale chimneys. *J. Wind Eng. Ind. Aerod.* 171, 353–365.
- Matteoni, G., Georgakis, C.T., 2012. Effects of bridge cable surface roughness and cross-sectional distortion on aerodynamic force coefficients. *J. Wind Eng. Ind. Aerod.* 104, 176–187.
- Mehmood, A., Nayfeh, A.H., Hajj, M.R., 2014. Effects of a non-linear energy sink (NES) on vortex-induced vibrations of a circular cylinder. *Nonlinear Dynam.* 77 (3), 667–680.
- Paidoussis, M.P., 2006. Real-life experiences with flow-induced vibration. *J. Fluid Struct.* 22 (6–7), 741–755.
- Paidoussis, M.P., Price, S.J., De Langre, E., 2010. Fluid-structure Interactions: Cross-Flow-Induced Instabilities. Cambridge University Press.
- Pavlovskaya, E., Keber, M., Postnikov, A., Reddington, K., Wiercigroch, M., 2016. Multi-modes approach to modelling of vortex-induced vibration. *Int. J. Non Lin. Mech.* 80, 40–51.
- Pettigrew, M.J., Taylor, C.E., 2003. Vibration analysis of shell-and-tube heat exchangers: an overview—Part 2: vibration response, fretting-wear, guidelines. *J. Fluid Struct.* 18 (5), 485–500.
- Sarpkaya, T., 2004. A critical review of the intrinsic nature of vortex-induced vibrations. *J. Fluid Struct.* 19, 389–447.
- Tumkur, R.K.R., Calderer, R., Masud, A., Pearlstein, A.J., Bergman, L.A., Vakakis, A.F., 2013a. Computational study of vortex-induced vibration of a sprung rigid circular cylinder with a strongly nonlinear internal attachment. *J. Fluid Struct.* 40, 214–232.
- Tumkur, R.K.R., Domany, E., Gendelman, O.V., Masud, A., Bergman, L.A., Vakakis, A.F., 2013b. Reduced-order model for laminar vortex-induced vibration of a rigid circular cylinder with an internal nonlinear absorber. *Commun. Nonlinear Sci. Numer. Simulat.* 18 (7), 1916–1930.
- Trim, A.D., Braaten, H., Lie, H., Tognarelli, M.A., 2005. Experimental investigation of vortex-induced vibration of long marine risers. *J. Fluid Struct.* 21 (3), 335–361.
- Vakakis, A.F., Manevitch, L.I., Gendelman, O., Bergman, L., 2003. Dynamics of linear discrete systems connected to local, essentially non-linear attachments. *J. Sound Vib.* 264 (3), 559–577.

- Violette, R., De Langre, E., Szydlowski, J., 2007. Computation of vortex-induced vibrations of long structures using a wake oscillator model: comparison with DNS and experiments. *Comput. Struct.* 85 (11–14), 1134–1141.
- Wang, J., Wierschem, N.E., Spencer Jr., B.F., Lu, X., 2015. Track nonlinear energy sink for rapid response reduction in building structures. *J. Eng. Mech.* 141 (1), 04014104.
- Wang, J., Wang, B., Wierschem, N.E., Spencer Jr., B.F., 2020. Dynamic analysis of track nonlinear energy sinks subjected to simple and stochastic excitations. *Earthq. Eng. Struct. Dynam.* 49 (9), 863–883.
- Wierschem, N.E., Luo, J., Al-Shudeifat, M., Hubbard, S., Ott, R., Fahnestock, L.A., Quinn, D.D., McFarland, D.M., Spencer Jr., B.F., Vakakis, A., Bergman, L.A., 2014. Experimental testing and numerical simulation of a six-story structure incorporating two-degree-of-freedom nonlinear energy sink. *J. Struct. Eng.* 140 (6), 04014027.
- Williamson, C., Govardhan, R., 2008. A brief review of recent results in vortex-induced vibrations. *J. Wind Eng. Ind. Aerod.* 96, 713–735.
- Wu, T., Kareem, A., 2012. An overview of vortex-induced vibration (VIV) of bridge decks. *Front. Struct. Civ. Eng.* 6, 335–347.
- Xu, K., Dai, Q., Bi, K., Fang, G., Zhao, L., 2022. Multi-mode vortex-induced vibration control of long-span bridges by using distributed tuned mass damper inertiors (DTMDIs). *J. Wind Eng. Ind. Aerod.* 224, 104970.
- Xue, Z., Han, B., Zhang, H., Xin, D., Zhan, J., Wang, R., 2021. External suction-blowing method for controlling vortex-induced vibration of a bridge. *J. Wind Eng. Ind. Aerod.* 215, 104661.
- Zdravkovich, M.M., 1981. Review and classification of various aerodynamic and hydrodynamic means for suppressing vortex shedding. *J. Wind Eng. Ind. Aerod.* 7 (2), 145–189.
- Zhang, M., Øiseth, O., Xu, F., 2021. Laminar flow-induced vibration of a three-degree-of-freedom circular cylinder with an attached splitter plate. *Phys. Fluids* 33 (11), 113605.
- Zhang, M., Øiseth, O., Petersen, Ø.W., Wu, T., 2022a. Experimental investigation on flow-induced vibrations of a circular cylinder with radial and longitudinal fins. *J. Wind Eng. Ind. Aerod.* 223, 104948.
- Zhang, M., Song, Y., Abdelkefi, A., Yu, H., Wang, J., 2022b. Vortex-induced vibration of a circular cylinder with nonlinear stiffness: prediction using forced vibration data. *Nonlinear Dynam.* 108 (3), 1867–1884.
- Zhang, M., Wu, T., Xu, F., 2019. Vortex-induced vibration of bridge decks: describing function-based model. *J. Wind Eng. Ind. Aerod.* 195, 104016.
- Zhang, M., Xu, F., 2022. Tuned mass damper for self-excited vibration control: optimization involving nonlinear aeroelastic effect. *J. Wind Eng. Ind. Aerod.* 220, 104836.
- Zhang, M., Xu, F., Øiseth, O., 2020. Aerodynamic damping models for vortex-induced vibration of a rectangular 4: 1 cylinder: comparison of modeling schemes. *J. Wind Eng. Ind. Aerod.* 205, 104321.
- Zhu, H., Gao, Y., 2017. Vortex-induced vibration suppression of a main circular cylinder with two rotating control rods in its near wake: effect of the rotation direction. *J. Fluid Struct.* 74, 469–491.